Geoscience Frontiers 12 (2021) 101074

HOSTED BY

Contents lists available at ScienceDirect

Geoscience Frontiers

journal homepage: www.elsevier.com/locate/gsf

Research Paper

Fetkin-hydro, a new thermo-hydrological algorithm for low-temperature thermochronological modeling

Francisco Sánchez [a,*], Andres Barrea [b], Federico M. Dávila [a], Andres Mora [c]

[a] Centro de Investigaciones en Ciencias de la Tierra (CICTERRA), CONICET-UNC, FCEFyN, Ciudad Universitaria, Av. Vélez Sarsfield 1611, 5000 Córdoba, Argentina
[b] Facultad de Matemática, Astronomía, Física y Computación (FAMAF), Ciudad Universitaria, Av. Medida Allende 2144, 5000 Córdoba, Argentina
[c] Ecopetrol, Botafogo, Rio de Janeiro, Brazil

ARTICLE INFO

Article history:
Received 30 January 2021
Received in revised form 22 July 2020
Accepted 1 September 2020
Available online 2 October 2020

Editor: E. Shaji

Keywords:
Thermochronology
Hydrogeology
Fluid flow
Numerical modeling

ABSTRACT

Despite two decades of major advances in the field of thermochronological modeling, state-of-the-art numerical implementations still rely mostly on burial and exhumation processes to explain radiometric measurements. Even though such an approach has proved valuable, failing to account for other first-order geological variables has led to misinterpretations and therefore, calls for a refinement. In this study a new version of the Fetkin (finite element temperature kinematics, Ecopetrol) program is presented. Its new algorithm couples time-dependent hydrological and thermal calculations, thus rendering thermochronological ages that, instead of being solely dependent on the kinematical evolution of a system, conditioning by the fluid flow is also present. In contrast with previous thermochronological models, this work considers the influence of effective stress on rock properties (porosity and permeability) and therefore, in thermal conductivity. Sensitivity analyses addressing relevant geological questions show not only the versatility of the code but also, new perspectives on forward low-temperature thermochronological modeling. Groundwater circulation through pure-sandstone settings produce colder thermal architectures than those obtained in impermeable domains. Differences in cooling ages from models with and without fluid circulation are up to 5 Myr. A 4-fold variation in thrusting rates (0.5 km/Myr to 2 km/Myr) produces a 15-Myr difference in cooling ages in models with fluid flow, which contrasts to much lower differences, only 2 Myr, in domains without (or minimal) fluid circulation. 2D thermal solutions in fold-bend-fold thrust belts composed of sandstones remain static despite substantial relief development by kinematic folding. A case-study from Western Argentina, in the Andean Precordillera, confirms the plausibility of the numerical algorithm here posed and raises new questions on the first-order thermal controls in settings under deformation.

1. Introduction

Thermochronological modeling has become critical for the assessment of orogenic processes and erosion rates (Zapata et al., 2019; Lossada et al., 2020; Wang et al., 2020), providing valuable insights of time-temperature paths of rocks in different tectonic settings (Carrapa and DeCelles, 2015; Mahoney et al., 2019; McDannell et al., 2019). It has also been used for predicting hydrocarbon maturation and kinematic reconstructions (Mora et al., 2015; Patiño et al., 2019; Schneider and Issler, 2019). However, thermochronological modeling still relies on assumptions that may challenge the applicability of the technique in some cases (Ehlers, 2005). Particularly, the general assumption that thermal advection is only caused by rock movements (faulting, erosion and deposition), neglects the effects of ubiquitous fluid flow.

Despite the fact that previous studies have (1) demonstrated the relevance of fluid flow on the thermal history, particularly in scenarios with simple topographies (Bethke, 1985; Forster and Smith, 1986, 1988, 1989; Ge and Garven, 1992); and (2) estimated the advective overprinting caused by underground flows (Lipsey et al., 2016; Leary et al., 2017; Przybycin et al., 2017; Chen et al., 2018, and references therein; Gessner et al., 2018; Tao et al., 2020), no thermochronological modeling approach has fully incorporated, to date, the contribution of time-dependent hydrological processes to the numerical algorithms. Recent works recognized the steady-state influence of fluid movement on Apatite Fission Track (AFT) and Apatite U-Th-Sm/He (AHe) ages (e.g., Whipp Jr and Ehlers, 2007; Luijendijk, 2019), but they received little further attention. The thermal effects of fluid circulation have neither been linked to structural kinematic models; a crucial tool for tying deformation to cooling ages (see Ketcham et al., 2018). For example, the relationship among deformation algorithms (e.g. fault-bend and fault-propagation folding; Suppe, 1983; Suppe and Medwedeff, 1990; Erslev, 1991), underground fluid flow, thermal state and cooling ages;

* Corresponding author.
E-mail addresses: nassif.franciscosanchez@gmail.com (F. Sánchez), andres.barrea@unc.edu.ar (A. Barrea), andres.mora@ecopetrol.com.co (A. Mora).

https://doi.org/10.1016/j.gsf.2020.09.005

is unknown. It should be noted that all modeling efforts seeking to relate hydrological and thermal calculations have considered a static spatial configuration, thus the implications of orogenic processes (i.e. time-dependent topography) have not been unveiled, or even discussed.

Forward numerical thermochronological studies have neglected regional effects of groundwater circulation on the basis of a conductive regime only sensitive to the kinematic history of the setting being assessed and mostly, to the basal heat flow (Patiño et al., 2019). Therefore, these studies excluded interpretation of samples proximal to fault zones, where effects of fluid circulation might substantially perturb radiometric ages (see for instance Nóbile et al., 2015). This work presents the first low-temperature thermochronological model coupling balanced structural sections with time-dependent thermal and hydrological calculations. The developed model presented not only complements the existing models, all of them only related to burial and exhumation (Braun, 2003; Ehlers, 2005), but also provides the unique opportunity to assess geological settings where major fluid circulation occurs, such as hydrothermal basins, high-rainfall regions, and others.

This paper presents a stepwise understanding from the theoretical background to case study implementation. Firstly, central equations concerning both the physical model and the numerical implementation (hereon referred to as Fetkin-hydro) are summarized (see Appendix for more information). Secondly, the workflow of the Fetkin-hydro program (see also Almendral et al., 2015) is reviewed to illustrate how input and output data are managed. Followed by, the effects of groundwater circulation under different regimes are assessed, by deploying some synthetic cases with a fault-bend fold geometry. Finally, the use of Fetkin-hydro in a real case scenario, the fold and thrust belt of the Argentine Precordillera, whereby low-temperature thermochronological systems are modeled with, and without, the effects of water circulation.

2. Theory

Assuming the fluid and rock matrix are in thermal equilibrium, the time dependent formulation for heat transfer, taking into account the effects of conduction, advection, and sink/sources; is given in

$$\frac{\partial T}{\partial t}\rho_b C_b = \nabla\cdot(\lambda\nabla T) - \left(q_f\rho_f C_f\cdot\nabla T\right) - (q_r\rho_r C_r\cdot\nabla T) + H \quad (1)$$

where T is temperature, t is time, λ is the thermal conductivity tensor characterizing the whole porous rock system, ρ_b and C_b are the bulk and specific heat capacity, respectively, q_f is the fluid velocity, obtained by a Darcian approximation, and q_r is the rock velocity, determined by the tectonic history of the setting. ρ_f and C_f correspond to fluid density and fluid heat capacity and ρ_r and C_r are the rock density and rock heat capacity, respectively. H represents heat sources and sinks, which for simplicity, were not included in the cases considered here.

Flow through porous media was considered in terms of the piezometric head, given in

$$S_0\frac{\partial h}{\partial t} + \nabla\cdot(K\nabla h) = G \quad (2)$$

where h denotes piezometric head, K is the ease with which fluid flows through the void space, (i.e. hydraulic conductivity), t denotes time, and G the fluid production. S_0, or specific storativity, corresponds to the volume of water released from (or added to) storage in a unit volume of porous medium, per unit change in the piezometric head.

Fluid velocities, obtained from solving equations on fluid flow (see Appendix for further details), are inserted into the heat Eq. (1) to obtain the thermal architecture. State variables (piezometric head and temperature) are calculated via the finite element method (Zienkiewicz, 1977; see Appendix). Parameters and constants used are shown in Table 1, following Hantschel and Kauerauf (2009) and Bear and Verruijt (2012).

The program deploys a mixed Eulerian-Lagrangian approach for overburden calculations, using third-party software structural information input. Irregularly-spaced structural data (points representing the spatial disposition of strata, hereon referred to as material points) is interpolated to the user-defined Eulerian grid at each time step, and vertical rock-load is obtained following the procedure depicted in Fig. 1. The procedure consists of interpolating material (Lagrangian) points to the fixed (Eulerian) grid and then using the vertical distance between them to calculate the weight of the rock column they bound (see Fig. 1B). Computation of overburden is followed by calculation of the effective stress and porosity (see Appendix). The algorithm handles some physical values including effective stress, hydraulic head, fluid velocities and temperature; at the fixed, Eulerian grid level (Fig. 1C). In contrast, a Lagrangian approach is used to track porosity and rock velocities (Fig. 1C). The code interchanges values from one level to another, i.e. from Eulerian to Lagrangian and viceversa, by considering the smallest Euclidean distance.

Table 1
Parameters used in the models. Values after Hantschel and Kauerauf (2009) and Bear and Verruijt (2012).

Parameter	Value	Units
Water density	1040	kg/m^3
Water specific heat	4186	J/(kg K)
Water thermal conductivity	0.64	W/mK
Shale compaction parameter	0.096	1/MPa
Shale initial porosity	0.7	
Shale density	2700	kg/m^3
Shale thermal conductivity	1.64	W/mK
Shale specific heat	860	J/(kg K)
Sandstone compaction parameter	0.026	1/MPa
Sandstone initial porosity	0.41	
Sandstone density	2720	kg/m^3
Sandstone thermal conductivity	3.95	W/mK
Sandstone specific heat	855	J/(kg K)

3. Methodology

3.1. Program overview

This section synthetizes the main aspects of Fetkin-hydro, including data input, workflow, and visualization of results. Further details can be found in Almendral et al. (2015).

As stated above, the main purpose of the program is to solve, both spatially and temporally, the thermal field of a geological setting under deformation. For such purpose, a series of balanced structural sections obtained from tectonic reconstructions, and an XML file specifying parameters and boundary conditions, are required. Files specifying the topographic surface and the upper piezometric head (water table), used to impose the upper thermal boundary condition and the upper head boundary condition, are also needed (Figs. 1, 2). A Dirichlet-type boundary condition is applied at the top and bottom boundaries, and a Newman-type condition, imposing no thermal or fluid flow across the side boundaries, is applied at the lateral boundary limits (Fig. 1B). Finally, the positions of the low-temperature thermochronological samples are specified in a tab-delimited text file that is also inputted to the program.

The algorithm assumes that the model evolves from a thermally and hydrologically equilibrated state, under which a linear increment of temperature from top to bottom and a unified piezometric head for the whole region, occur simultaneously. In order to calculate the porosity-dependent overburden (see Appendix for details), the program first obtains the porosity field assuming hydrostatic, depth-conditioned compaction (see Hantschel and Kauerauf, 2009). After the initial "guess" of mechanical compaction, the program calculates the porosity-dependent overburden and the effective-stress state of the region. Then, the code computes a second approximation of the rock porosities, this time from an effective-stress law (Terzagui, 1923; see

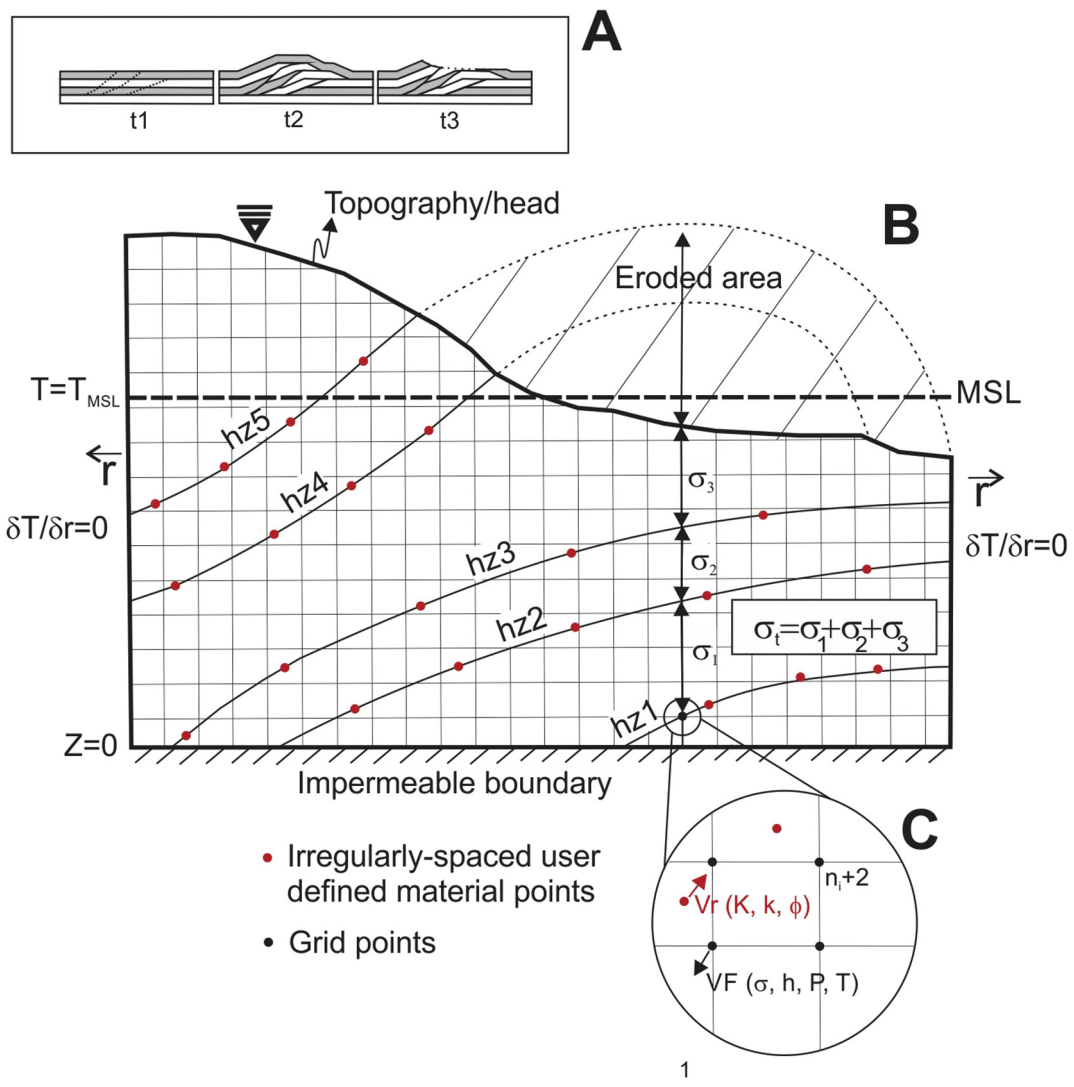

Fig. 1. Model setup and space discretization considered in Fetkin-hydro. See text for notation.

Appendix) and not from hydrostatic depth. From this step, the time iteration takes place (Fig. 2). Considering the time stepping imposed by the user, the program marches in forward sense solving the temperature and fluid flow equations (see Section 2; Theory). Fluid velocities are obtained from the latter, and are used in the subsequent time iteration to calculate thermal advection related to fluid flow. *Re*-gridding is performed at each iteration, as the fixed Eulerian grid "shrinks" or "stretches" in order to fully cover the region bounded by the time-evolving topographic surface and the bottom of the model. Under completion of all iterations the program writes a series of output files containing information of the finite element numerical process (e.g. node locations, triangulation order), the numerical results at each time step (temperature, heads, porosities, hydraulic conductivities, fluid velocities) as well as modeled low-temperature thermochronological ages, and vitrinite (%Ro) reflectance (optional). While thermochronological ages can be readily plotted, analysis of the thermal and hydrological solutions may require use of triangulation routines, as the software returns modeled values at the triangle-nodes and not at a rectangular Eulerian grid. This can be accomplished by a series of MATLAB scripts (see details in Almendral et al., 2015), written to visualize and compare results from different case studies.

3.2. Numerical tests

To complement previous views concerning the thermal evolution of settings such as fold and thrust belts (Husson and Moretti, 2002; Huerta and Rodgers, 2006; among others), different numerical experiments considering a typical fault-bend fold model (see Huerta and Rodgers, 2006; Lock and Willett, 2008; Almendral et al., 2015) were performed. These results not only illustrate the benefits of the code presented, but also bring forward a discussion on major variables that need to be considered when modeling cooling ages. The kinematic experiments involve a thrust system on which slip occurs from right to left at a 1 km/Myr rate. Materials involved in deformation are considered homogeneous and isotropic, thus hydraulic and thermal properties are equivalent in the x and y axis for all nodes. The thrust ramp dips with 30°, with flats being located at 15 km and 5 km below surface. Deformation starts at 10 Myr and continues to the present day (0 Myr). Lithological properties are described in Table 1. The upper boundary condition, along the surface, was set to 20 °C, whereas the basal temperature, at 30 km depth, was 600 °C. Atmospheric lapse rate was set to 4 °C/km, and heat production was not considered. An arbitrary inherited age of 30 Myr was chosen for all samples across the topographic relief, in

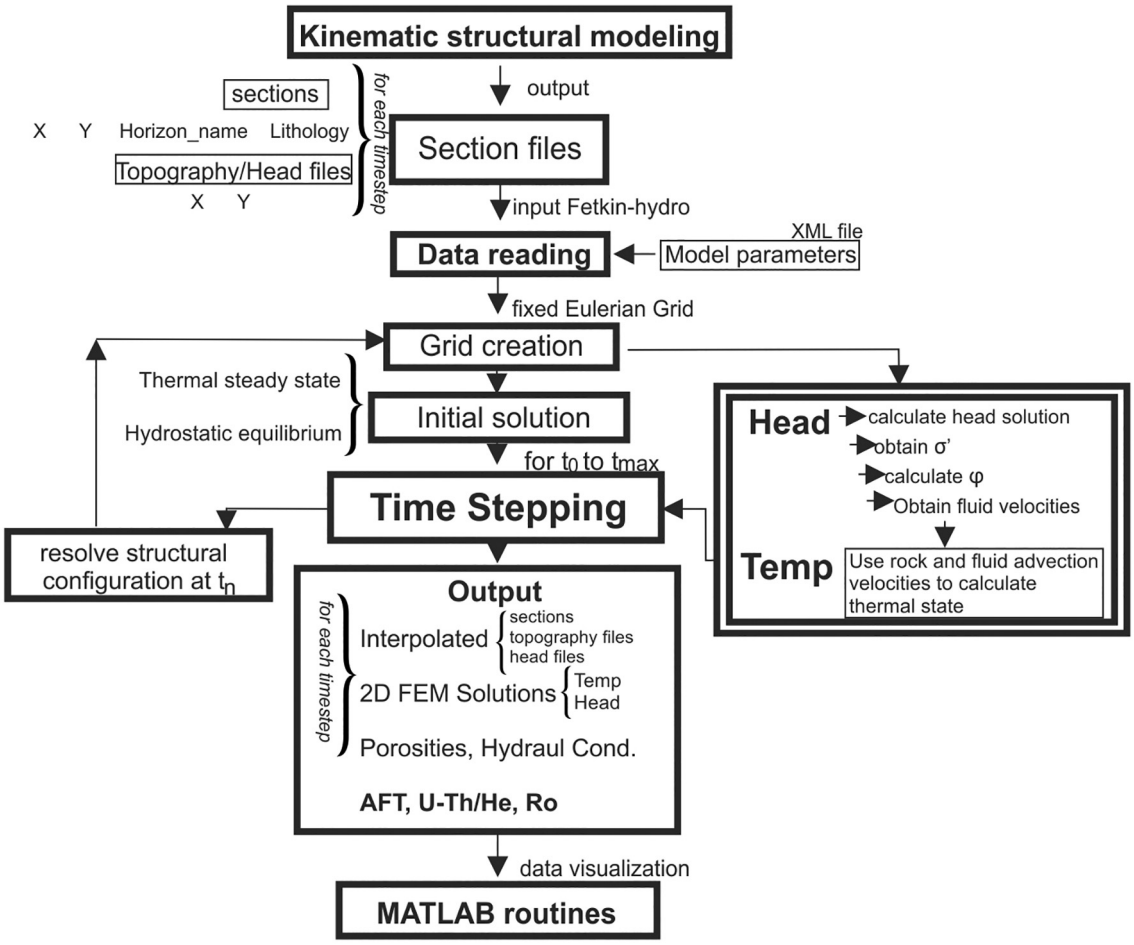

Fig. 2. Workflow of Fetkin-hydro.

order to easily distinguish reset ages from the unreset ones. AHe and AFT ages were modeled in each experiment (see Reiners and Ehlers, 2005, for further reading).

Impact of lithology on the solutions (temperature and piezometric head) is addressed in first place; by performing numerical tests involving a permeable (sandy) domain and an impermeable (shale) one. Following this, experiments assessing the effects of fault permeability, thrusting rate and erosion, are performed; taking into account the two lithological end members (permeable and impermeable) previously considered. To simulate the effects of erosion in a deforming thrust belt (see Huerta and Rodgers, 2006; Almendral et al., 2015), the program solves

$$\frac{\partial h}{\partial t} = V_{\text{rock}_y} + V_{\text{rock}_x}\frac{\partial h}{\partial x} - k_e|x_r|^m\left|\frac{\partial h}{\partial x}\right|^n \quad (3)$$

where h denotes elevation, t is time, V_{rock_y} and V_{rock_x} are the rock velocities in the y and x-axis, respectively; k_e is the erodibility parameter and x_r the distance from the drainage divide, recalculated at each time step (Bernal et al., 2018). The elevation of the water divide was also corrected following Eq. (3), after erosion in neighboring points had been computed. The m and n parameters (related to erosion) were set to one (see Huerta and Rodgers, 2006).

4. Results

4.1. Lithology

Fig. 3A and B show results for two contrasting lithological scenarios: sandstone-dominated (see Fig. 3A; hereon called case 1) and shale-dominated (see Fig. 3B; hereon called case 2). A standard Fetkin thermo-kinematic model considering standard rock physical parameters and no fluid flow (Almendral et al., 2015) is also shown for comparison (see Fig. 3B-d; case 3). For cases 1 and 2, the evolution (for 10 million years) of temperature, piezometric head, and porosity was calculated. For case 3 only thermal history is shown, as such model does not involve fluid flow computations.

In Case 1 (Fig. 3A) isotherms (see Fig. 3A-a) do not accompany the deformation-driven relief development, giving evidence for a relatively stable thermal architecture during the modeled time lapse. In fact, temperatures beneath the fold crest do not follow the expected trend, in which isotherms mimic the topographic profile (Stüwe et al., 1994; Husson and Moretti, 2002). Following this, the region beneath the crest is hereon called the "thermal depression". For the cases 2 and 3 (Fig. 3B-a, and B-d, respectively), in contrast, the isotherms evolve concurrent to the generation of topography, evidencing temperature changes during the relief generation occasioned by folding. Evolution and dynamics of the piezometric head within the modeled pore space differ substantially between permeable and impermeable domains (notice arrows in Fig. 3A-b and B-b, depicting fluid direction). While in case 1 the flow circulation occurs outward the deformation region (upwarping area, showing a fanned geometry); in case 2 the flow occurs inward, evidencing mostly vertical movements. The white contours in Fig. 3A-b and B-b outline isopiezometric heads, displayed with the purpose of illustrating the fluid flow pattern from higher (bright) to lower (dark) piezometric head regions. Findings from cases 1 and 2 clearly evidence the strong control of lithological properties on the hydrological regime, and ultimately, on the fluid flows and temperatures. Model results for case 3 (Fig. 3B-d) appear similar with respect to the

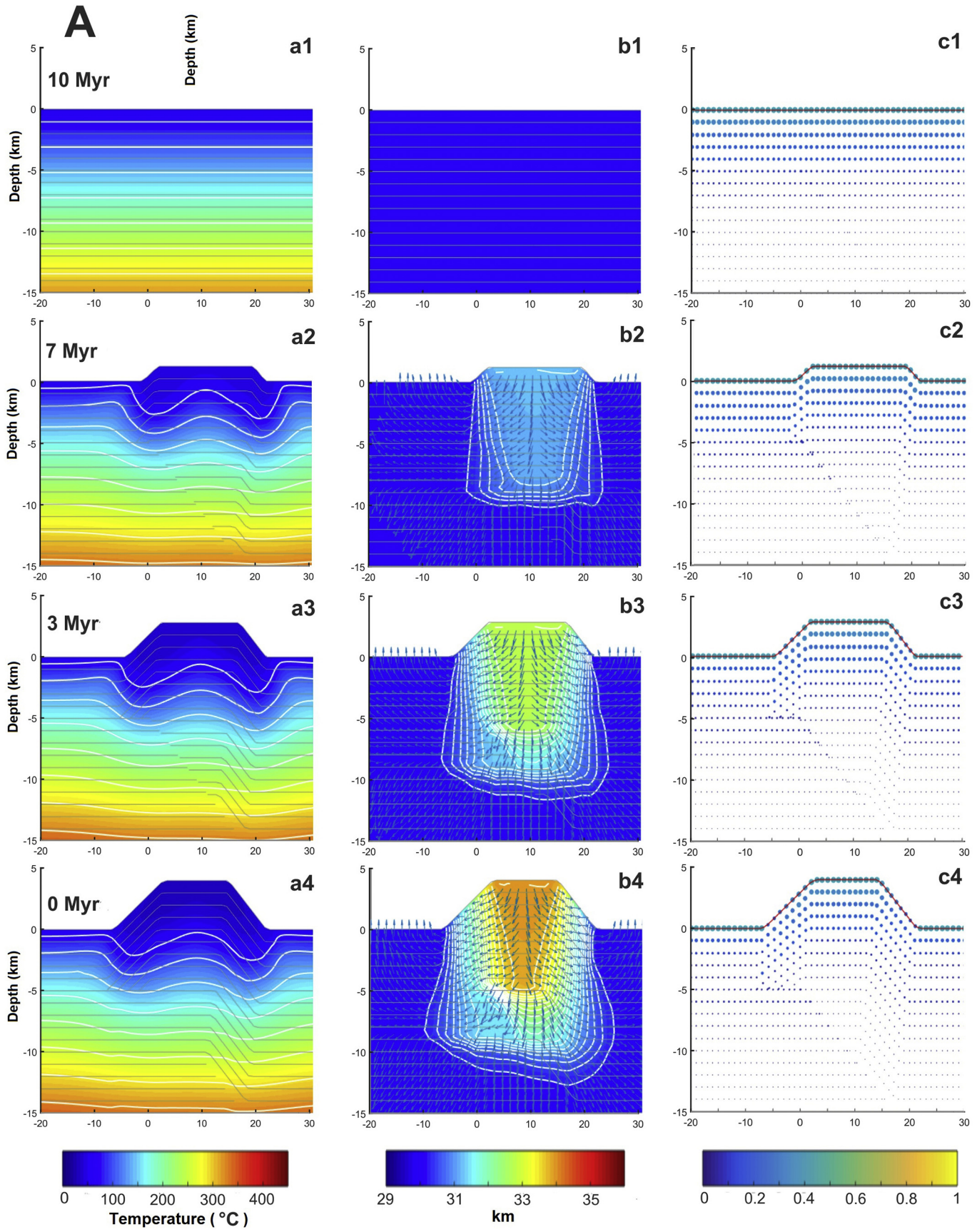

Fig. 3. (A) Model results for a pure-sandstone sequence. Thermal (a) and hydrological (b) states, along with rock-porosities (c; scaled in both size and color), are shown for 10, 7, 3 and 0 Myr (present day). White lines depict contours of temperature and head values. Red line in c denotes the topographic surface. (B) Model results for a pure-shale sequence and a no-fluid model (bottom). Thermal (a) and hydrological (b) states, along with rock-porosities (c; scaled in both size and color), are shown for 10, 7, 3 and 0 Myr (present day). White lines depict contours of temperature and head values. Red line in c denotes the topographic surface. Inset d shows thermal results for a model without fluid circulation. (C) Rock permeability for the two lithological end-members considered. (D) Predicted ages for the U-Th/He and Apatite Fission Track systems.

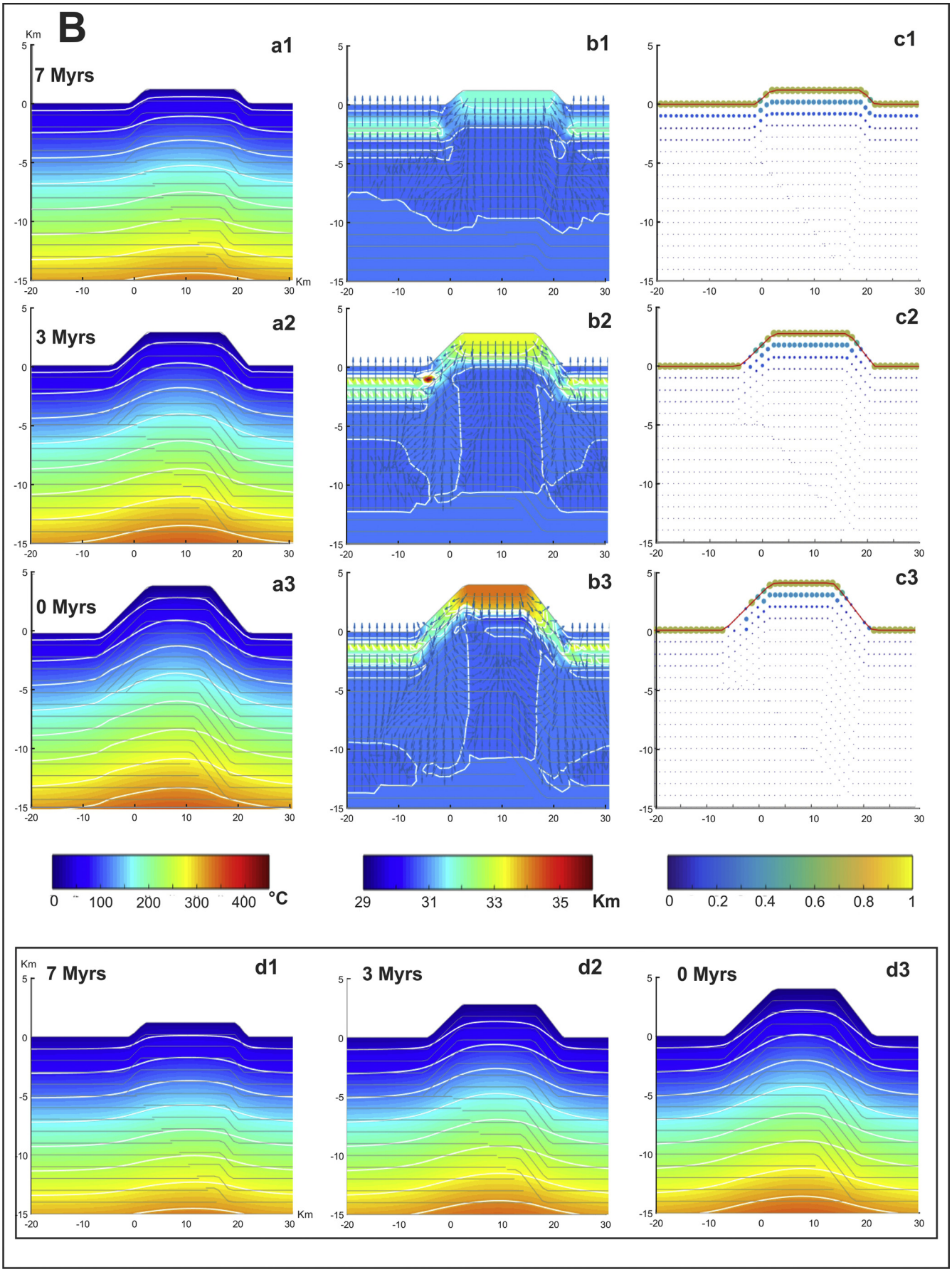

Fig. 3 (*continued*).

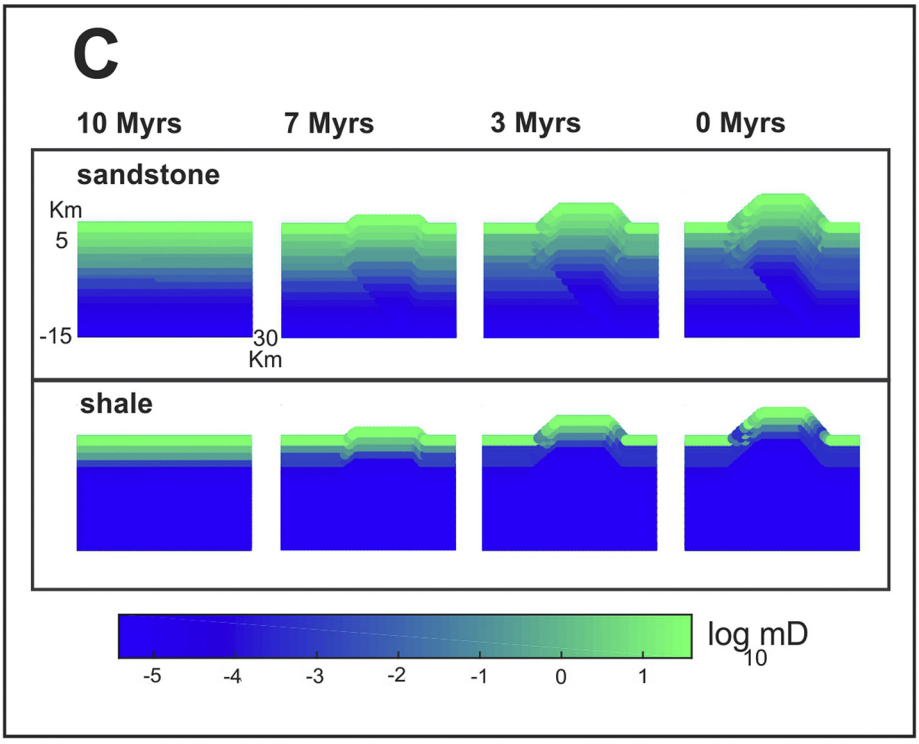

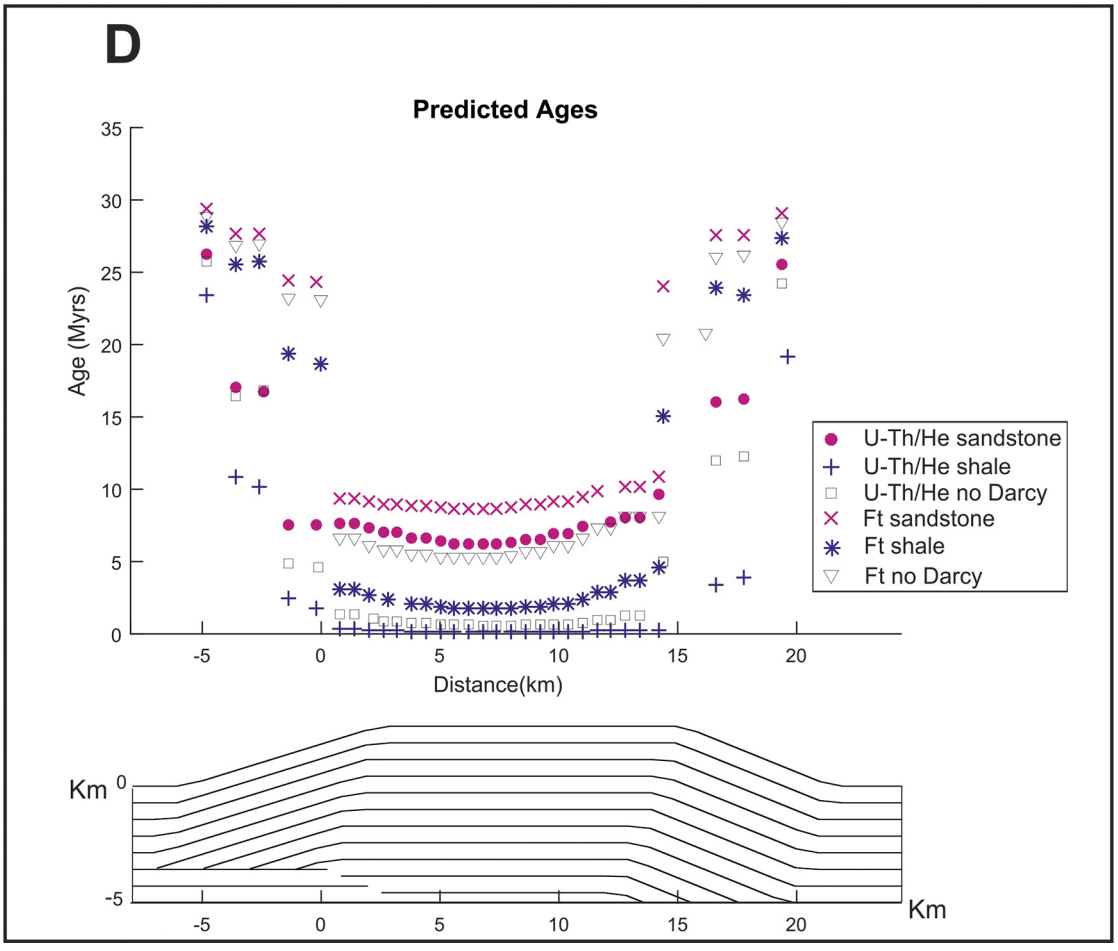

Fig. 3 (*continued*).

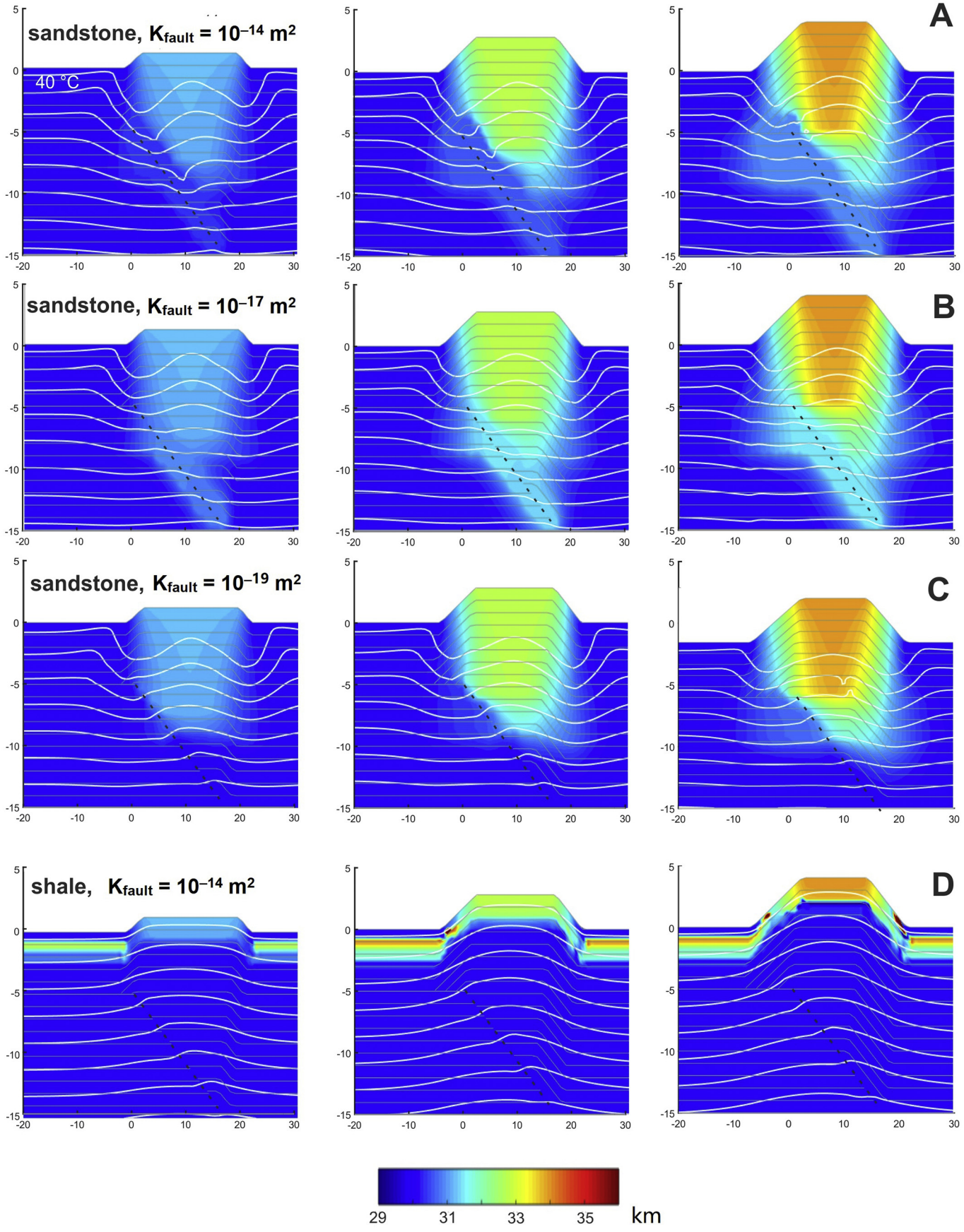

Fig. 4. Model results considering different fault permeabilities. White contours denote isotherms at each 40 °C increment. Color scale depicts piezometric head. Black dashed lines represent fault location.

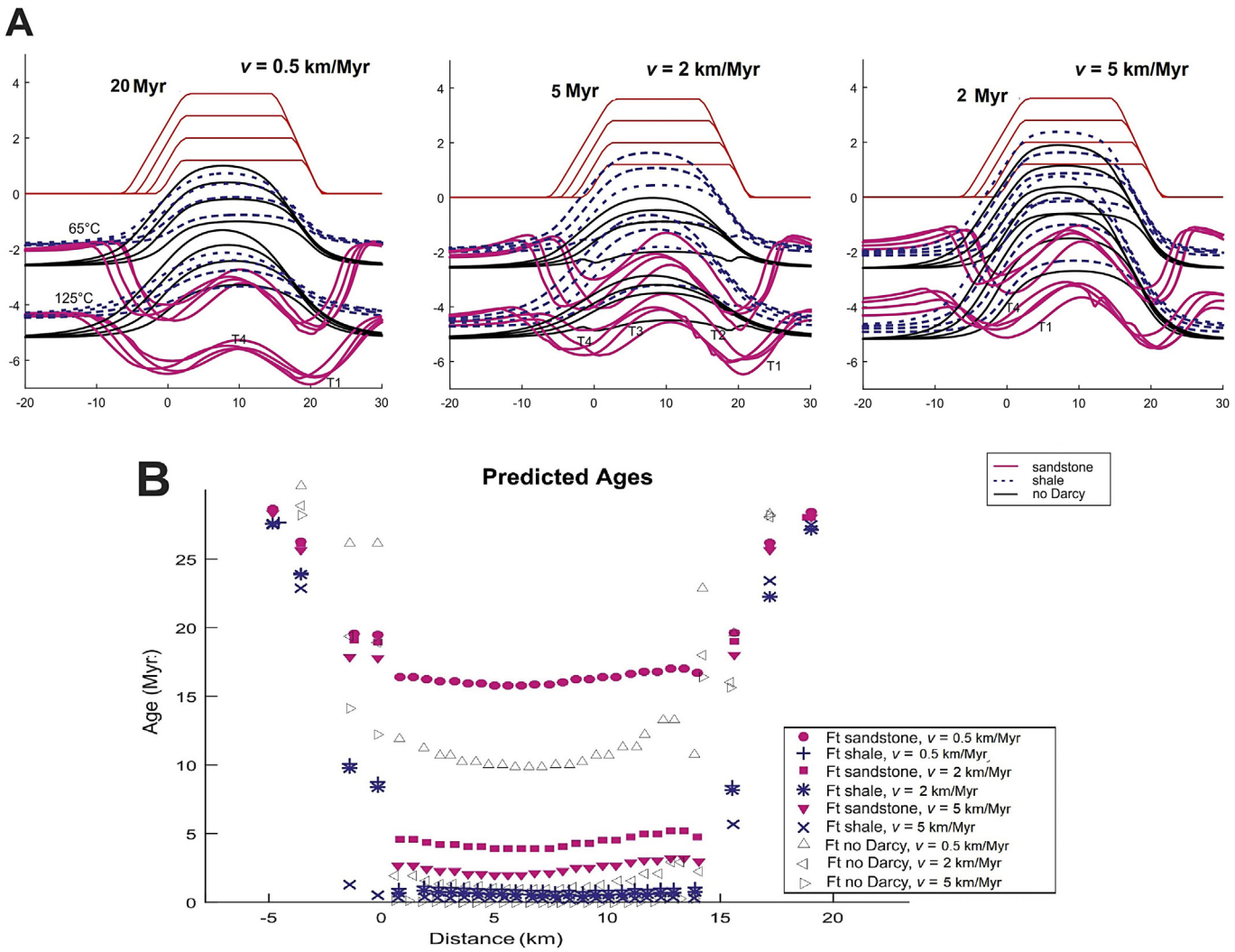

Fig. 5. (A) Model results considering different thrusting velocities. Magenta, blue and black lines represent isotherms for sandstone-dominated settings, shale-dominated settings and no fluid flow model, respectively. Red line denotes topography at different times (see text). (B) Modeled Fission track ages for the different thrusting velocities considered.

impermeable scenario (case 2, Fig. 3B-a), which can be ascribed to the absence of groundwater circulation.

Calculated rock porosities are shown in Fig. 3A-c and B-c, which are scaled in both color and size for readability. Porosities for surficial rocks were always maintained at the initial value, which depends on the lithology considered (Table 1). As porosity (and thus, permeability) was allowed to vary according to the effective stress, the values did not remain constant throughout the simulation. Rock porosities for the sandy domain remain around 30% for shallow depths (< 4 km, see Fig. 3A-c1 to A-c4). Rock compaction in shales occurs at a higher rate, and only surficial rocks located at the crest of the anticline maintain porosities around 20% (Fig. 3B-c1 to B-c3). The increase in piezometric head at the shallow levels, as an effect of the moving head boundary condition (which moves apace with the topographic profile) prevents the porous space from shrinking. This leads to a net reduction in effective stress, since overburden does not overcome the (indeed augmenting) pore pressure. In regards to the porosity-dependent permeability, the values for the two end-members studied are shown in Fig. 3C. An intermediate class of permeability (10^{-3} to 10^{-6} D) was obtained for the sandy domains at shallow ranges (< 5 km), while values spanning from low-permeability to impermeable were attained at deeper levels for the two end-member lithological cases. Such permeability ranges imply that the values here considered are scaled in geological time and are suitable for the time intervals concerned by this work (Ungerer et al., 1990). The two permeability profiles obtained for the lithologies considered (see Fig. 3C), represent a major benefit of adopting an effective-stress/porosity relationship and not a depth/porosity one.

Modeled thermochronological ages along the x-axis are shown in Fig. 3D. All samples were taken at a constant depth y = 0, thus disclosing insights of the thermal evolution across the thrust-related fold without recurring to erode it. Modeled samples from sandstone rocks are shown in magenta colors, shale rocks in blue, and samples derived from a model with no Darcian circulation appear colorless. The modeled samples exhibit a "U-shape" along the modeled fault-bend-fold (Huerta and Rodgers, 2006; Almendral et al., 2015), which occurs as an effect of the thrust geometry considered and the enforced boundary conditions. Samples with approximately 0 Myr for the U-Th/He system are still hotter than their respective closure isotherm. As expected from the previous examination of the evolving thermal field (Fig. 3A,B), samples from sandstone environments exhibit older ages than those retrieved from impermeable conditions (shales). In contrast, those taken from shaly domains yield younger ages than their non-Darcian analogous settings. The two lithological end-members considered (sandstones and shales) might suggest that fluid flow could impact low-temperature cooling ages in two possible ways: promoting aging in highly conductive, permeable environments; or promoting rejuvenation in

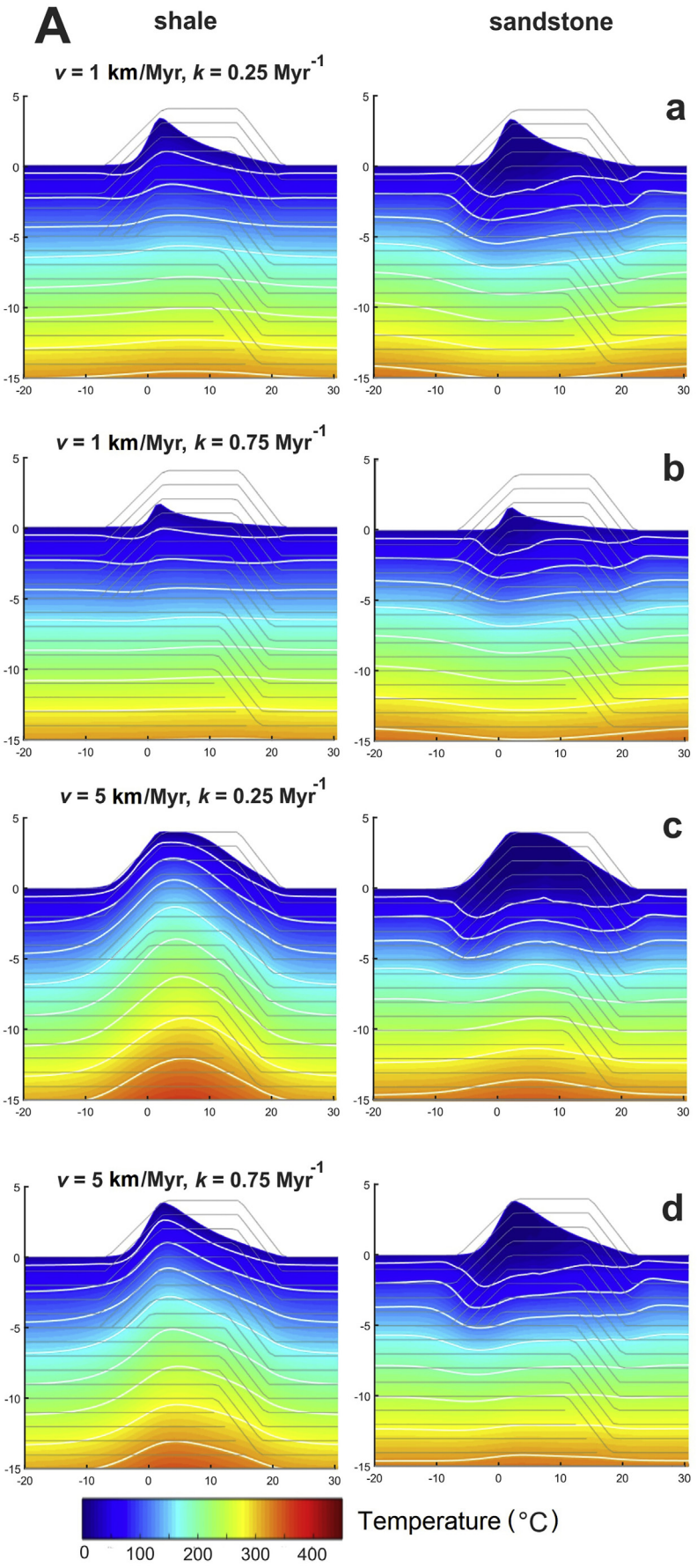

Fig. 6. (A) Model results for different erosion scenarios. (B) Modeled fission track ages for the different erosion scenarios considered.

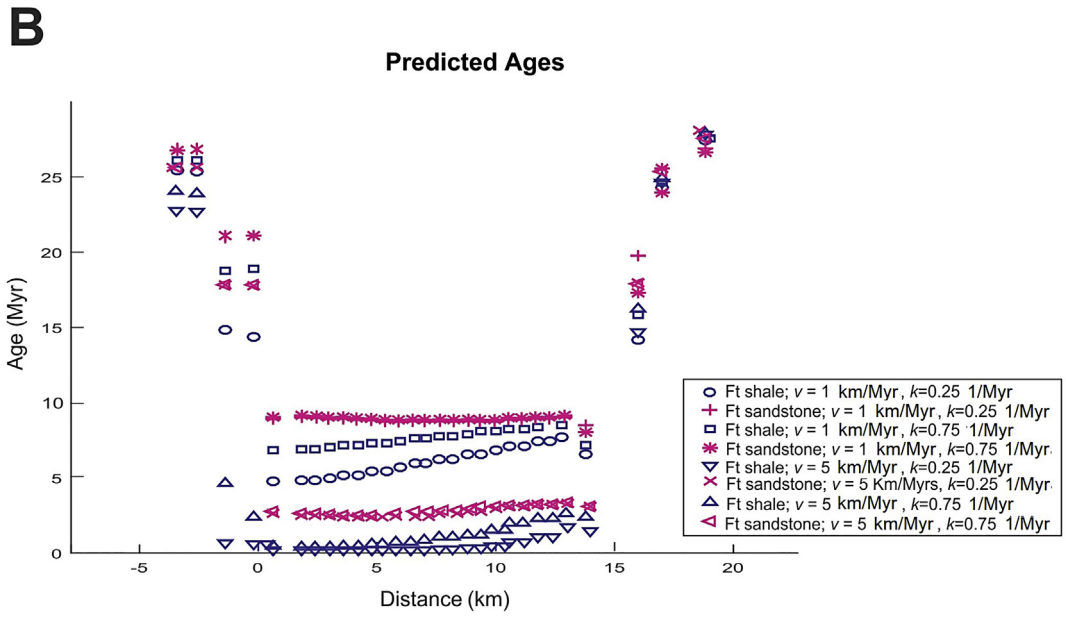

Fig. 6 (*continued*).

impermeable settings. Such conclusions can be sustained for the two systems modeled (AHe and AFT).

4.2. Fault permeability

Fig. 4 shows how changes in fault permeability (from 10^{-14} m^2 to 10^{-19} m^2) affect the fluid flow distribution (represented by piezometric head values) and temperature. It can be pointed that fluid circulation across the thrust zone (dashed lines in Fig. 4) for a sandstone-dominated environment, may not be directly correlated with fault permeability; as a progressive increase in fault permeability (from 10^{-19} m^2 to 10^{-14} m^2) does not necessarily promote water circulation (i.e. higher piezometric heads, Fig. 4A–C). Groundwater circulation for the shale scenario does not vary according to fault permeability (see Fig. 4D).

The temperature profiles adjust according to the permeability of the fault, exhibiting a peak-valley shape along the fault location (see isotherms, white lines, near the fault zone). Consistent with results from Forster and Smith (1989), the extent of the thermal perturbation associated with the fault location is mainly controlled by the relationship between the fault and rock permeability, and not by the absolute value of the fault permeability itself. Forster and Smith (1989) proposed the existence of a "permeability window", i.e., a combination of rock and fault permeability that maximize surficial thermal perturbations. Our results are rather similar to those reported by Forster and Smith (1989) even though our model setups consider a range of permeabilities for the deforming rocks instead of one. Although a highly permeable fault induces a quick disturbance on the thermal and fluid regimes along the fault (see Fig. 4A), the existence of such perturbation hampers diffusion of temperature and water masses at later stages. In comparison, a lesser permeable fault (see Fig. 4B) could promote larger fluid circulation, which implies that fluid flow across a fault is not controlled solely by the value of fault permeability. Regarding cooling ages, our findings suggest that short-lived thermal perturbations, as those caused by flow through narrow permeable conduits (see Fig. 4), may have no major implications on thermochronological measurements. It should be noted that even the extreme permeability case of $K_{fault} = 10^{-14}$ m^2 causes no substantial changes on the ages compared to the previous cases (Fig. 3D), where the permeabilities of the fault and the surrounding rock were the same. Modeled ages considering fault permeability differed from the previous experiment (Fig. 3D) by less than 0.5 Myr, and therefore are not shown. Fault permeability however, may play a more important role when the fault serves as a contact surface between two different materials, since the permeability of the fault itself would determine the amount of fluid what would infiltrate from one media to another.

4.3. Thrusting velocity

This section considers the influence of thrusting velocities on low-temperature thermochronological cooling ages, considering rates of 0.5 km/Myr, 2 km/Myr and 5 km/Myr; and the two litholotical end-member scenarios previously studied (i.e., shales and sandstones, see Fig. 5A, magenta lines represent sandstones and blue lines shales). Experiments addressing thrusting velocity allow contrasting results from this work with previous studies performed under no fluid flow conditions (e.g., Huerta and Rodgers, 2006). Fig. 5A displays closure isotherms for both AHe and AFT systems (~65 °C and 125 °C, respectively) at 3, 5, 7, and 10 Myr, abbreviated as T1, T2, T3 and T4. Given the similarity between the AHe and AFT age patterns along the x-axis (see Fig. 3D), only AFT results are shown for discussion.

Despite the fact that the upper boundary condition moves upward as a consequence of fault-bend-folding, thermal solutions for sandstone-dominated sequences do not vary substantially along the vertical axis. For these cases (sandstone), the isotherms move laterally in the direction of deformation (see magenta isotherms, all cases). This implies a major difference with impermeable shales and "dry" environments (see blue and black lines, respectively), where isotherms are displaced to shallower positions as deformation evolves, accompanying the relief creation. This observation has been also documented by semi-analytical (Stüwe et al., 1994) and numerical (Husson and Moretti, 2002; Braun, 2003) efforts. Furthermore, the thermal solution posed in this work for permeable (sandstone) environments might cast new insights regarding the evolution of temperature in deforming systems.

Modeling of low-temperature thermochronological cooling ages with varying thrusting velocities (see Fig. 5B) show that isotopic samples from permeable rocks are more susceptible to changes in deformation rates than samples extracted from impermeable scenarios. Furthermore, permeable rocks show a typical U-profile, aging-rejuvenating-aging, which flattens (plateau ages) across the deformed area, where the cooling ages

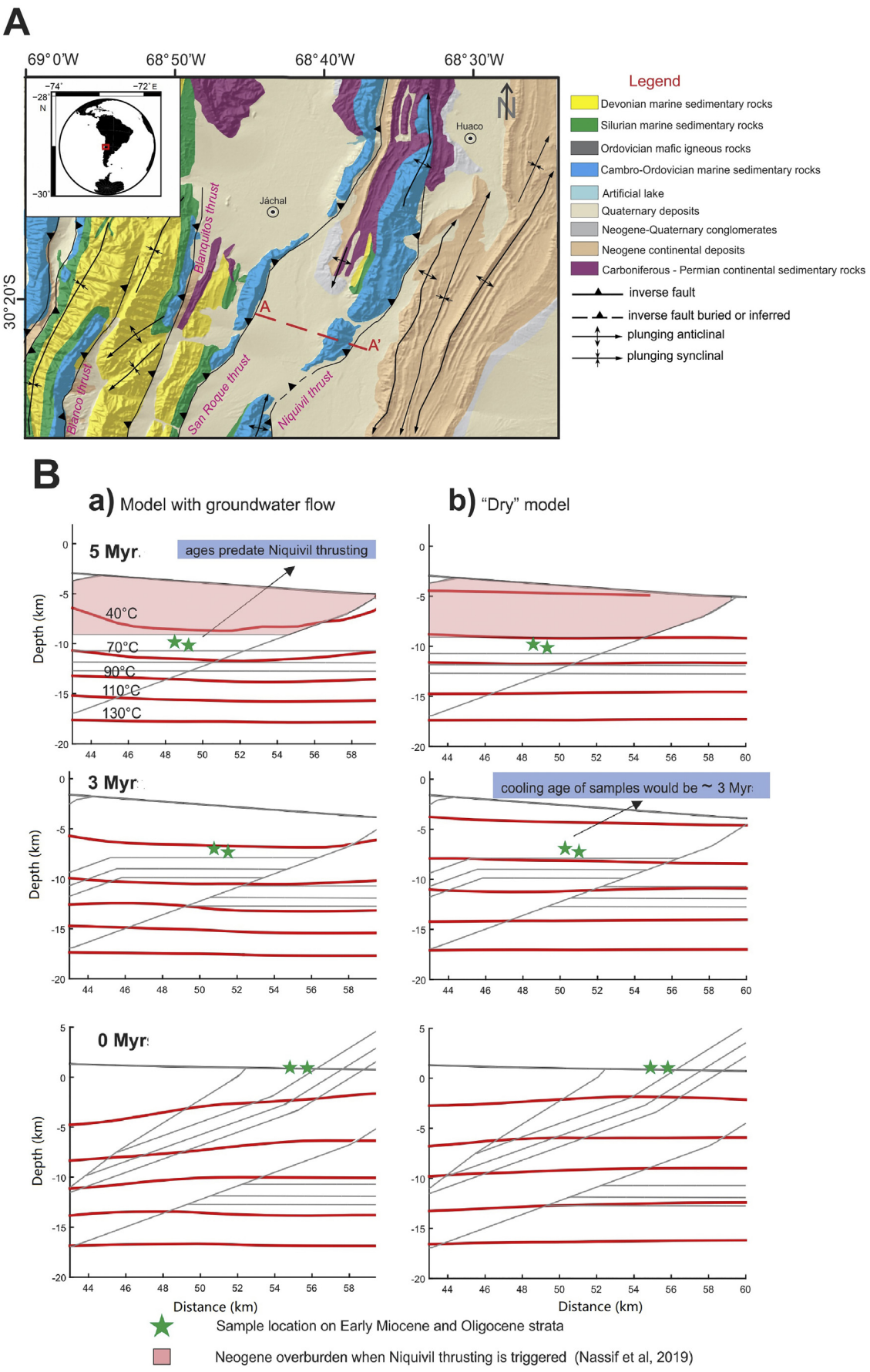

Fig. 7. (A) Geological map of the study region (modified after Nassif et al., 2019; structural and geological data after Allmendinger and Judge, 2014). (B) Results for the real-case scenario for fluid flow and "dry" models.

are the youngest. The degree of such age flattening is related to the slowness of thrusting deformation. It is important to note that the lowest thrusting rate (e.g., 0.5 km/Myr, see Fig. 5A) yields the oldest modeled age. As expected from examination of Fig. 5A, the lowest deformation rate considered yields the coldest environment and, because of no reheating, also the oldest thermochronological ages (see Fig. 5A, B). In addition, these results corroborate previous findings regarding youthening/aging of samples, as permeable environments under deformation yield considerably older ages than the ones obtained from a model without, or minimal (impermeable settings) Darcian circulation.

4.4. Erosion

Results considering erosion show that isotherms accompany the relief creation in a thrust system formed entirely by shales (Fig. 6A), analogous to cases where fluid circulation is not taken into account (see Huerta and Rodgers, 2006; Almendral et al., 2015). This effect, known as "thermal bulge" (Huerta and Rodgers, 2006), has been interpreted to be caused by heat production from decaying radioactive elements in the crust or thermal advection of moving thrust sheets (Husson and Moretti, 2002). In addition, the upper boundary condition imposed along the topographic profile may also cause such thermal perturbation, as thermal equilibrium in the system would render a linear increase in temperature from top to bottom, adjusting the temperature according to the elevation of topography for each position along the x-axis. Similar to our previous results (Figs. 3A and 5A), sandstone-dominated thrust systems subject to erosion also develop a "thermal depression", independent of deformation or erosion rates. In contraposition to impermeable settings, where the thermal field is conditioned by the topographic growth, modeled temperatures in permeable experiments suggest that effects of deformation are preserved even after the structures have been almost completely removed by erosion (see Fig. 6A-d). Additionally, sandstone dominated sequences develop an asymmetric thermal solution, whereby the "depressed" isotherms move towards the foreland side of the growing anticline (see Fig. 6A, sandstone cases).

Fig. 6B shows the cooling age distribution for the different erosion rates and rock permeabilities considered. The age flattening effect within permeable domains, previously associated with slowness of deformation (thrusting velocity experiment, see Section 4.3), does not vary with the erosion parameter (see overlapping values for a fixed thrusting velocity in Fig. 6B). This is consistent with the observation (see above) that thermal perturbations related to deformation-driven topography creation seem to be preserved even after such relief has been partially or even totally removed. Our results indicate that in permeable domains (sandstones), a flattened profile could be retrieved instead of the expected U-shape. Such flattening is attributed to the existence of the "thermal depression" (discussed previously, see Section 4.1; Lithology), which counteracts the effects of fault-bend-fold kinematics that would otherwise produce a concave-up profile. Results for impermeable rocks are in accordance with previous numerical experiments without fluid flow, i.e., a U-shape profile, modified by the effects of erosion. In addition, the erosion parameter in impermeable domains is coupled with age, as older ages are obtained by increasing the erosion parameter for a fixed thrusting velocity. However, the erosion parameter might not be a first-order variable regarding cooling ages of impermeable rocks (nor permeable ones, as already seen), since a 3-fold variation in k (from 0.25 to 0.75), only produces differences of ~1 Myr.

4.5. Real case scenario

In this section Fetkin-Hydro was used to model a real thrust-system case in western Argentina (~30°S), the Argentine Precordillera (AP), located in the Pampean-Chilean flat-slab segment of the southern Central Andes (see Fig. 7A). It is a typical fold-and-thrust belt (Allmendinger and Judge, 2014; Levina et al., 2014; Nassif et al., 2019) and, likely, one of the thrust systems most studied in the world. Its landscape configuration (today) shows meridional and sub-parallel thrust sheets separated by major thrust faults; which have been associated with a deep decollement (~16 km). It is composed of N-S trending mountains that record a prolonged Paleozoic to Cenozoic tectonic history, suggested to be controlled by accretion of exotic terranes (Ramos et al., 1986) and the subduction of the Nazca plate beneath the South American lithosphere (Isacks et al., 1982; Jordan et al., 1983a, 1983b). The AP constitutes an ideal natural laboratory to analyze the relationship between deformation and low-temperature thermochronological cooling ages. The region not only provided excellent structural and geo- and thermo- chronology data sets to analyze this connection (see Fosdick et al., 2015; Nassif et al., 2019 and references therein) but also stratigraphic and sedimentologic approaches to support our interpretations (Jordan et al., 2001; Levina et al., 2014).

Recent low-temperature thermochronological studies in the AP, particularly (U—Th)/He and fission track analysis; have provided new insights on the tectonic evolution of the thrust belt during the Andean orogeny (Fosdick et al., 2015). These were interpreted in terms of exhumation, burial, and uplift episodes; under a thermal history only conditioned by the geodynamic regime of the region (and the consequent thermal input from below; see Fosdick et al., 2015). A flat subduction has been proposed to affect the AP since ~20–15 Ma to present (see Ramos and Folguera, 2009 and references therein). The thermal effects of this subduction regime have been, in turn, associated with a cold thermal scenario across western and central Argentina (with geotherms <20 °C/km, see Collo et al., 2011, 2017). Using the agreed structural kinematic reconstructions (see Allmendinger et al., 1990; Jordan et al., 1993; Allmendinger and Judge, 2014; Nassif et al., 2019), the reported cooling ages (see Fosdick et al., 2015) were modeled with Fetkin-hydro. Focus was placed on the easternmost Precordillera thrust sheet, known as Niquivil thrust sheet, which is bounded by the San Roque and Niquivil thrusts to the West and East, respectively (see Fig. 7A). AHe data in Niquivil (on Silurian and Oligocene strata) provided ages ~15 Ma and 8 Ma, suggesting that cooling ages would be prior to thrusting (constrained between ~5 Ma and today; see Jordan et al., 1993; Allmendinger and Judge, 2014; Nassif et al., 2019). Such thermochronological ages imply that, despite the substantial burial experienced by Silurian and Oligocene rocks during the last 5 Myr (see kinematic reconstructions available to date; Nassif et al., 2019), the maximum temperatures reached by those intervals could not have surpassed the closure temperature of the AHe system, i.e., ~60 °C (see Reiners and Ehlers, 2005). If that were the case, AHe ages would yield younger values than the Niquivil fault thrusting age (5 Myr).

Following the conditions stated above, numerical experiments without ("dry") and with ("wet") groundwater flow were performed. It is important to note that recent studies have shown the presence of groundwater (both meteoric and formational; see Lynch and van der Pluijm, 2017) in the AP, which demonstrates the plausibility of incorporating fluids in our model. Lithological characterization followed Allmendinger and Judge (2014), hydrological and thermal properties were assigned after Hantschel and Kauerauf (2009), and paleotopography was taken from the (only) available model to date (Nassif et al., 2019). Thermal income to the base of the model was taken from Fosdick et al. (2015), that on the basis of inverse thermal modeling constrained the temperatures experienced by Silurian strata of the AP thrusts (i.e., the units involved in deformation). Basal and surface temperatures were set to 150 °C and 20 °C, respectively; and a Newman condition of no energy and fluid mass transfer was imposed at the model boundaries.

Given that measured AHe ages are older than the Niquivil's thrusting age, it is not possible to find a thermo-kinematic-hydrological solution that correlates deformation with thermochronology. Following this, the thermal environment required to leave the sampled rocks unreset was modeled, which implied that any inherited thermochronological age considered before deformation should remain unchanged after thrusting (i.e., deformation along Niquivil thrust did not affect the inherited cooling ages). This exercise constituted a challenging

enterprise, as an important *syn*-thrusting sedimentation (~6 km thick, see Nassif et al., 2019) contemporaneous with the timing of the Niquivil thrust (Jordan et al., 1993; Allmendinger and Judge, 2014; Nassif et al., 2019), could have reset the low-temperature AHe isotopic system. It is remarked that under average geothermal gradient conditions, the temperature at 6 km might be ~200 °C.

Fig. 7B shows results for both models, with and without fluid flows (Fig. 7B-a and B-b, respectively). The initial position of Oligocene and lower Miocene samples at 5 Myr, under ~6 km of sediments (Nassif et al., 2019), might imply thermal resetting of low-temperature thermochronological systems. The "dry" model (without fluid flows) produces thermal resetting, providing cooling ages ~3 Myr (see Fig. 7B-b), as the samples would have crossed the AHe closure temperature (~60 °C) at that time. Such results are not in accordance with reported results in this thrust sheet (cooling ages between 15 Myr and 8 Myr, see Fosdick et al., 2015). In contrast, the model with fluid flow (Fig. 7B-a) is consistent with the reported cooling ages as well as with the kinematic and structural reconstructions in the region. Since the thermal state for the model with groundwater flow is substantially colder than the "dry" scenario (see the position of the 40 °C isotherm in Fig. 7B-a), Oligocene and lower Miocene strata always remain above the closure isotherm, conserving their inherited thermochronological ages. Results for the model with fluid circulation suggest that the thermal architecture nowadays is still affected by groundwater movement through the sandstone-rich Neogene strata. This is consistent with previous hydrological assessments in the area; at the easternmost AP (see Pesce and Miranda, 2003; Lynch and van der Pluijm, 2017).

The modeled cooling ages yielded by the no-fluid-flow model (Fig. 7B-b), could only fit measured cooling ages by reducing the temperature at the base of the model (i.e., thermal gradient at the beginning of the simulation). In comparison, the model with fluid flows suggests that extremely-low geothermal gradients (<5 °C/km) are not required to explain cooling ages, since the presence of the topographically-driven flow across the Niquivil thrust sheet might explain the cold (< 25 °C/km) scenario. This hydrological-induced cooling, only disclosed by the model where groundwater movement is taken into account, hampered thermal resetting of the AHe system and preserved the inherited ages within the Niquivil thrust sheet. In summary, our results suggest that modeling of the unsteady hydrological system, and its coupling with the evolving thermal architecture, may provide central insights to the analysis of thermochronological records, as shown here for the case of the Argentine Precordillera.

5. Discussion

Results from our work complement previous insights on low-temperature thermochronological modeling and the effects of fluid circulation on the temperature field and cooling ages. Trends in AHe and AFT ages along a classic fold-and-thrust belt differ from the ones without incorporating fluid circulation through the pore space (see Huerta and Rodgers, 2006; Almendral et al., 2015). In sandy domains the "thermal bulge" along the fault plane (see Huerta and Rodgers, 2006) is not reproducible, obtaining instead surficial temperatures that do not mimic the topographic surface. This finding is consistent with previous steady-state simulations that took into account fluid flow (Bethke, 1985; Ge and Garven, 1992), but contradicts observations asserting that the influence of the topographic profile should decay exponentially with depth (Turcotte and Schubert, 2002). This implies that in basins where water recharge by rainfall is ensured (see upper boundary condition for hydrological calculations in Section 2, Theory), effects of relief on the thermal architecture might be overestimated. Furthermore, given that models accounting for topography-driven fluid flow might render colder environments than those obtained in "dry" scenarios, higher basal temperatures that fit thermal observations can be posed. However, the geological complexity of hydrological basins calls for a careful assessment of boundary conditions (Bear and Verruijt, 2012; and references therein), and further efforts addressing detailed analyses of boundary enforcements are needed to complement the insights aforementioned.

Our results suggest that Darcian circulation influences the thermal evolution as much as other first order variables such as kinematic evolution or basal heat flow. This might prompt for a revision of thermochronological models in settings where groundwater circulation is appreciable, especially in hydrothermal basins. In such settings not only large volumes of fluids are in play, but also, the temperature of such fluids might vary depending on the pattern of hydrological circulation in the basin (for example, groundwater might be heated in underground aquifers). As suggested by Tao et al. (2020) understanding circulation paths of underground fluids might be crucial to constrain the thermal state of the shallow crust.

Future application of Fetkin-hydro to realistic settings still faces some drawbacks which include: paleo positions of the water-table, required by the algorithm to deploy hydrological calculations, might be difficult to constrain in some regions and; the porosity-permeability model used in this version might not fit data from well-logs or field measurements; which might be better explained by data-driven porosity-permeability laws (see also Appendix for further details). Nonetheless, the algorithm presented here will allow users to obtain insights on the evolution of low-temperature thermochronological systems involving both fluid flow and deformation, such as the Argentine fold-and-thrust belt utilized in this work. Extension to other settings (i.e. multiple faults, trishear folding, subsiding basins, etc.) and model enhancement (consideration of horizontal shear-stresses, incorporation of newer permeability models; (see Appendix), will be the subject of future works.

6. Conclusions

Fetkin-hydro is a new version of the Fetkin simulator incorporating fluid flow calculations. By coupling thermal and hydrological equations, Fetkin-hydro provides new perspectives on the evolution of basins, whose thermal regimes might have been inaccurately modeled by previous numerical algorithms that did not account for groundwater circulation through porous media. The versatility and applicability of the code, that now incorporates fluid flow, are shown through a series of sensitivity analyses which address relevant geological questions such as the linking between erosion and thrusting kinematics. Low-temperature Apatite Fission Track and U-Th/He thermochronological systems are modeled in different scenarios, yielding insights of the influence of fluid movement on radiogenic ages. Successful integration of the program with data from a world-known thrust belt, the Argentine Precordillera, proves the plausibility of the numerical algorithm posed here. The present work complements previous efforts aimed at understanding the thermal evolution of geological settings under structural deformation, and sets new questions on the first-order phenomena that should be taken into account for modeling low-temperature thermochronological systems.

Declaration of Interest

The authors declare that they have no known competing financial interests or personal relationships that could have appeared to influence the work reported in this paper.

Acknowledgments

We appreciate funding from FONCyT (PICT funding program), SECyT-UNC, CONICET, PUE-CICTERRA 2016, PICT-E 2018.

Appendix A. Supplementary data

Supplementary data to this article can be found online at https://doi.org/10.1016/j.gsf.2020.09.005.

References

Allmendinger, R.W., Judge, P.A., 2014. The argentine Precordillera: A foreland thrust belt proximal to the subducted plate. Geosphere 10 (6), 1203–1218.

Allmendinger, R.W., Figueroa, D., Snyder, D., Beer, J., Mpodozis, C., Isacks, B.L., 1990. Foreland shortening and crustal balancing in the Andes at 30 S latitude. Tectonics 9 (4), 789–809.

Almendral, A., Robles, W., Parra, M., Mora, A., Ketcham, R.A., Raghib, M., 2015. FetKin: Coupling kinematic restorations and temperature to predict thrusting, exhumation histories, and thermochronometric ages. AAPG Bull. 99 (8), 1557–1573.

Bear, J., Verruijt, A., 2012. Modeling Groundwater Flow and Pollution. 2. Springer Science & Business Media.

Bernal, A., Hardy, S., Gawthorpe, R., 2018. Three-Dimensional growth of Flexural Slip Fault-Bend and Fault-Propagation Folds and their Geomorphic Expression. Geosciences 8 (4), 110.

Bethke, C.M., 1985. A numerical model of compaction-driven groundwater flow and heat transfer and its application to the paleohydrology of intracratonic sedimentary basins. J. Geophys. Res. Solid Earth 90 (B8), 6817–6828.

Braun, J., 2003. Pecube: A new finite-element code to solve the 3D heat transport equation including the effects of a time-varying, finite amplitude surface topography. Comput. Geosci. 29 (6), 787–794.

Carrapa, Barbara, DeCelles, Peter G., 2015. Regional exhumation and kinematic history of the Central Andes in response to cyclical orogenic processes. Geol. Soc. Am. Mem. 212, 201–213.

Chen, Z., Grasby, S.E., Dewing, K., Osadetz, K.G., Brent, T., 2018. Geological controls on the present temperature field of the western Sverdrup Basin, Canadian Arctic Archipelago. Basin Res. 30, 479–496.

Collo, G., Dávila, F.M., Nóbile, J., Astini, R.A., Gehrels, G., 2011. Clay mineralogy and thermal history of the Neogene Vinchina Basin, Central Andes of Argentina: Analysis of factors controlling the heating conditions. Tectonics 30 (4).

Collo, G., Dávila, F.M., Teixeira, W., Nóbile, J.C., Sant Anna, L.G., Carter, A., 2017. Isotopic and thermochronologic evidence of extremely cold lithosphere associated with a slab flattening in the Central Andes of Argentina. Basin Res. 29 (1), 16–40.

Ehlers, T.A., 2005. Crustal thermal processes and the interpretation of thermochronometer data. Rev. Mineral. Geochem. 58 (1), 315–350.

Erslev, E.A., 1991. Trishear fault-propagation folding. Geology 19 (6), 617–620.

Forster, C., Smith, L., 1986. The Influence of Groundwater Flow on Thermal Regimes in Mountainous Terrain (No. SGP-TR-93-20). Ph.D. Thesis. Department of Geological Sciences, University of British Columbia, Vancouver, British Columbia, Canada.

Forster, C., Smith, L., 1988. Groundwater flow systems in mountainous terrain: 1. Numerical modeling technique. Water Resour. Res. 24 (7), 999–1010.

Forster, C., Smith, L., 1989. The influence of groundwater flow on thermal regimes in mountainous terrain: a model study. J. Geophys. Res. Solid Earth 94 (B7), 9439–9451.

Fosdick, J.C., Carrapa, B., Ortíz, G., 2015. Faulting and erosion in the argentine Precordillera during changes in subduction regime: Reconciling bedrock cooling and detrital records. Earth Planet. Sci. Lett. 432, 73–83.

Ge, S., Garven, G., 1992. Hydromechanical modeling of tectonically driven groundwater flow with application to the Arkoma foreland basin. J. Geophys. Res. Solid Earth 97 (B6), 9119–9144.

Gessner, K., Markwitz, V., Güngör, T., 2018. Crustal fluid flow in hot continental extension: tectonic framework of geothermal areas and mineral deposits in western Anatolia. Geol. Soc. Lond., Spec. Publ. 453 (1), 289–311.

Hantschel, T., Kauerauf, A.I., 2009. Fundamentals of Basin and Petroleum Systems Modeling. Springer Science & Business Media.

Huerta, A.D., Rodgers, D.W., 2006. Constraining rates of thrusting and erosion: Insights from kinematic thermal modeling. Geology 34 (7), 541–544.

Husson, L., Moretti, I., 2002. Thermal regime of fold and thrust belts—an application to the Bolivian sub Andean zone. Tectonophysics 345 (1–4), 253–280.

Isacks, B., Jordan, T., Allmendinger, R., Ramos, V.A., 1982. La segmentaci6n tect6nica de los Andes Centrales y su relaci6n con la placa de Nazca subductada. V Congr. Latinoamericano Geol, Buenos Aires, Actas, III, pp. 587–606.

Jordan, T.E., Lsacks, B., Ramos, V.A., Allmendinger, R.W., 1983a. Mountain building in the Central Andes. Episodes 3, 20–26.

Jordan, T.E., Isacks, B., Allmendinger, R., Brewer, J., Ramos, V.A., Ando, C., 1983b. Andean tectonics related to geometry of subducted plates. Geol. Soc. Am. Bull. 94 (3), 341–361.

Jordan, T.E., Allmendinger, R.W., Damanti, J.F., Drake, R.E., 1993. Chronology of motion in a complete thrust belt: the Precordillera, 30-31 S, Andes Mountains. J. Geol. 101 (2), 135–156.

Jordan, T.E., Schlunegger, F., Cardozo, N., 2001. Unsteady and spatially variable evolution of the Neogene Andean Bermejo Foreland Basin, Argentina. J. S. Am. Earth Sci. 14, 775–798.

Ketcham, R.A., Mora, A., Parra, M., 2018. Deciphering exhumation and burial history with multi-sample down-well thermochronometric inverse modelling. Basin Res. 48–64.

Leary, P., Malin, P., Niemi, R., 2017. Fluid flow and heat transport computation for power-law scaling poroperm media. Geofluids 2017.

Levina, M., Horton, B.K., Fuentes, F., Stockli, D.F., 2014. Cenozoic sedimentation and exhumation of the foreland basin system preserved in the Precordillera thrust belt (31–32 S), southern Central Andes, Argentina. Tectonics 33 (9), 1659–1680.

Lipsey, L., Pluymaekers, M., Goldberg, T., van Oversteeg, K., Ghazaryan, L., Cloetingh, S., van Wees, J.D., 2016. Numerical modelling of thermal convection in the Luttelgeest carbonate platform, the Netherlands. Geothermics 64, 135–151.

Lock, J., Willett, S., 2008. Low-temperature thermochronometric ages in fold-and-thrust belts. Tectonophysics 456 (3–4), 147–162.

Lossada, A.C., Hoke, G.D., Giambiagi, L.B., Fitzgerald, P.G., Mescua, J.F., Suriano, J., Aguilar, A., 2020. Detrital thermochronology reveals major middle Miocene exhumation of the eastern flank of the Andes that predates the Pampean flat-slab (33°-33.5° S). Tectonics 39 (4), e2019TC005764.

Luijendijk, E., 2019. Beo v1.0: numerical model of heat flow and low-temperature thermochronology in hydrothermal systems. Geosci. Model Dev. 12 (9), 4061–4073.

Lynch, E.A., van der Pluijm, B., 2017. Meteoric fluid infiltration in the argentine Precordillera fold-and-thrust belt: evidence from H isotopic studies of neoformed clay minerals. Lithosphere 9 (1), 134–145.

Mahoney, L., Mclaren, S., Hill, K., Kohn, B., Gallagher, K., Norvick, M., 2019. Late cretaceous to Oligocene burial and collision in western Papua New Guinea: Indications from low-temperature thermochronology and thermal modelling. Tectonophysics 752, 81–112.

McDannell, K.T., Schneider, D.A., Zeitler, P.K., O'Sullivan, P.B., Issler, D.R., 2019. Reconstructing deep-time histories from integrated thermochronology: an example from southern Baffin Island, Canada. Terra Nova 31 (3), 189–204.

Mora, A., Casallas, W., Ketcham, R.A., Gomez, D., Parra, M., Namson, J., Stockli, D., Almendral, A., Robles, W., Ghorbal, B., 2015. Kinematic restoration of contractional basement structures using thermokinematic models: A key tool for petroleum system modeling. AAPG Bull. 99 (8), 1575–1598.

Nassif, F.S., Canelo, H., Davila, F., Ezpeleta, M., 2019. Constraining erosion rates in thrust belts: Insights from kinematic modeling of the argentine Precordillera, Jachal section. Tectonophysics 758, 1–11.

Nóbile, J.C., Collo, G., Dávila, F.M., Martina, F., Wemmer, K., 2015. Successive reactivation of older structures under variable heat flow conditions evidenced by K–Ar fault gouge dating in Sierra de Ambato, northern argentine broken foreland. J. S. Am. Earth Sci. 64, 152–165.

Patiño, A.M., Parra, M., Ramírez, J.C., Sobel, E.R., Glodny, J., Almendral, A., Echeverri, S., 2019. Thermochronological constraints on cenozoic exhumation along the Southern Caribbean. In: Horton, B.K., Folguera, A. (Eds.), The Santa Marta Range, Northern Colombia. Andean Tectonics, pp. 103–132.

Pesce, A., Miranda, F., 2003. Catálogo de Manifestaciones Termales de la República Argentina. Vol. I-II Región Noroeste. SEGEMAR, Buenos Aires, pp. 1666–3462.

Przybycin, A.M., Scheck-Wenderoth, M., Schneider, M., 2017. The origin of deep geothermal anomalies in the German Molasse Basin: results from 3D numerical models of coupled fluid flow and heat transport. Geotherm. Energy 5 (1), 1.

Ramos, V.A., Folguera, A., 2009. Andean flat-slab subduction through time. Geol. Soc. Lond., Spec. Publ. 327 (1), 31–54.

Ramos, V.A., Jordan, T.E., Allmendinger, R.W., Mpodozis, C., Kay, S.M., Cortés, J.M., Palma, M., 1986. Paleozoic terranes of the central Argentine-Chilean Andes. Tectonics 5 (6), 855–880.

Reiners, P.W., Ehlers, T.A., 2005. Low-Temperature Thermochronology: Techniques, Interpretations, and Applications. 58. Walter de Gruyter GmbH & Co KG.

Schneider, D.A., Issler, D.R., 2019. Application of low-temperature thermochronology to hydrocarbon exploration. Fission-Track Thermochronology and its Application to Geology. Springer, Cham, pp. 315–333.

Stüwe, K., White, L., Brown, R., 1994. The influence of eroding topography on steady-state isotherms. Application to fission track analysis. Earth Planet. Sci. Lett. 124 (1–4), 63–74.

Suppe, J., 1983. Geometry and kinematics of fault-bend folding. Am. J. Sci. 283 (7), 684–721.

Suppe, J., Medwedeff, D.A., 1990. Geometry and Kinematics of fault-propagation folding. Eclogae Geol. Helv. 87, 33–46.

Tao, C., Seyfried, W.E., Lowell, R.P., Liu, Y., Liang, J., Guo, Z., Ding, K., Zhang, H., Liu, J., Qiu, L., Egorov, I., 2020. Deep high-temperature hydrothermal circulation in a detachment faulting system on the ultra-slow spreading ridge. Nat. Commun. 11 (1), 1–9.

Terzagui, V., 1923. Die Berechnung der Durchassigkeitsziffer des Tones aus dem Verlauf der hydrodynamischen Spannungs. erscheinungen. Sitzungsber. Akad. Wiss. Math. Naturwiss. Kl. Abt. 2A (132), 105–124.

Turcotte, D.L., Schubert, G., 2002. Geodynamics. Cambridge University Press.

Ungerer, P., Burrus, J., Doligez, B.P.Y.C., Chenet, P.Y., Bessis, F., 1990. Basin evaluation by integrated two-dimensional modeling of heat transfer, fluid flow, hydrocarbon generation, and migration (1). AAPG Bull. 74 (3), 309–335.

Wang, W., Zheng, D., Li, C., Wang, Y., Zhang, Z., Pang, J., Wang, Y., Yu, J., Wang, Y., Zheng, W., Zhang, H., 2020. Cenozoic exhumation of the Qilian Shan in the northeastern Tibetan Plateau: evidence from low-temperature thermochronology. Tectonics 39 (4), e2019TC005705.

Whipp Jr., D.M., Ehlers, T.A., 2007. Influence of groundwater flow on thermochronometer-derived exhumation rates in the central Nepalese Himalaya. Geology 35 (9), 851–854.

Zapata, S., Sobel, E.R., del Papa, C., Jelinek, A.R., Glodny, J., 2019. Using a paleosurface to constrain low-temperature thermochronological data: tectonic evolution of the cuevas range, Central Andes. Tectonics 38 (11), 3939–3958.

Zienkiewicz, O.C., 1977. The Finite Element Method. 3rd ed. McGraw Hill, London.